On the Rapid Intensification of Hurricane Wilma (2005). Part I: Model Prediction and Structural Changes

HUA CHEN, DA-LIN ZHANG, AND JAMES CARTON

Department of Atmospheric and Oceanic Science, University of Maryland, College Park, College Park, Maryland

ROBERT ATLAS

NOAA/Atlantic Oceanographic and Meteorological Laboratory, Miami, Florida

(Manuscript received 21 December 2010, in final form 4 April 2011)

ABSTRACT

In this study, a 72-h cloud-permitting numerical prediction of Hurricane Wilma (2005), covering its initial 18-h spinup, an 18-h rapid intensification (RI), and the subsequent 36-h weakening stage, is performed using the Weather Research Forecast Model (WRF) with the finest grid length of 1 km. The model prediction uses the initial and lateral boundary conditions, including the bogus vortex, that are identical to the Geophysical Fluid Dynamics Laboratory's then-operational data, except for the time-independent sea surface temperature field. Results show that the WRF prediction compares favorably in many aspects to the best-track analysis, as well as satellite and reconnaissance flight-level observations. In particular, the model predicts an RI rate of more than 4 hPa h^{-1} for an 18-h period, with the minimum central pressure of less than 889 hPa. Of significance is that the model captures a sequence of important inner-core structural variations associated with Wilma's intensity changes, namely, from a partial eyewall open to the west prior to RI to a full eyewall at the onset of RI, rapid eyewall contraction during the initial spinup, the formation of double eyewalls with a wide moat area in between during the most intense stage, and the subsequent eyewall replacement leading to the weakening of Wilma. In addition, the model reproduces the boundary layer growth up to 750 hPa with an intense inversion layer above in the eye. Recognizing that a single case does not provide a rigorous test of the model predictability due to the stochastic nature of deep convection, results presented herein suggest that it is possible to improve forecasts of hurricane intensity and intensity changes, and especially RI, if the inner-core structural changes and storm size could be reasonably predicted in an operational setting using high-resolution cloud-permitting models with realistic initial conditions and model physical parameterizations.

1. Introduction

The hurricane is one of the most dangerous natural hazards to human society and the environment. Thus, it is of great importance to accurately predict many hours in advance a hurricane's track, intensity, and rate of intensity change, as well as the associated torrential rainfall. Due to the complex nature of the physics involved in the development of hurricanes, our forecast capability depends highly on guidance provided by various numerical (dynamical and statistical) models. Although there have been continuing improvements in forecasting hurricane track and landfall location, very little progress has been seen in intensity forecasting during the past two decades (Marks et al. 1998; Rappaport et al. 2009).

Apparently, hurricane intensity change involves multiscale nonlinear interactions of different phenomena and variables (Marks et al. 1998; Shen et al. 2010). Such interactions include the sea surface temperature (SST), ocean heat content, vertical wind shear (VWS), environmental moisture, inner-core dynamics and thermodynamics, cloud microphysics, and air–sea interaction processes, which are not all well represented by today's hurricane models. Indeed, Rappaport et al. (2009) report that today's dynamical hurricane models have not reached the skill level of statistical intensity models in many cases. In particular, current hurricane models tend to underpredict very strong storms and overpredict very weak storms. Moreover, many inner-core structures, such as narrow spiral rainbands, small eye size, polygonal eyewalls, and eyewall replacement cycles (ERCs), cannot be

Corresponding author address: Dr. Da-Lin Zhang, Dept. of Atmospheric and Oceanic Science, University of Maryland, College Park, College Park, MD 20742-2425.
E-mail: dalin@atmos.umd.edu

DOI: 10.1175/WAF-D-11-00001.1

captured by current operational models. These inner-core structures appear to be closely related to intensity changes and the final intensity of hurricanes.

It has long been recognized that our ability to understand and predict hurricane intensity changes is hampered partly by the lack of realistic four-dimensional high-resolution data, and partly by deficiencies in hurricane models, including the model initial conditions. Earlier observational studies, based on the flight-level and satellite data, could only examine hurricane vortex structures and precipitation characteristics (e.g., Parrish et al. 1982; Marks and Houze 1987). Use of Doppler radar data can reveal many inner-core features, such as eyewall replacement morphology, and low-level wind variations over coastal and inland regions (e.g., Willoughby et al. 1982; Marks and Houze 1984; Bluestein and Hazen 1989; Blackwell 2000; Black and Willoughby 1992). Nevertheless, the lack of high-resolution observations often precludes a detailed analysis and description of structural changes, and the cause and effect of the underlying physical processes taking place in intensifying hurricanes. These structural changes appear to be closely related to significant intensity fluctuations and redistributions of precipitation and rotational winds in hurricanes (e.g., Hogsett and Zhang 2009).

On the other hand, considerable progress has been made in cloud-permitting simulations of hurricanes during the past 15 years (see Liu et al. 1997, 1999; Davis and Bosart 2001; Braun 2002; Rogers et al. 2003; Zhu et al. 2004; Yang et al. 2008). These studies have provided novel insights into the inner-core structures and evolutionary patterns of some hurricanes that are closely related to hurricane intensity changes. Using hurricane models at cloud-permitting scales ($\Delta x = 2$–6 km), it is now possible to reproduce reasonably well the asymmetric structures of the eye, the eyewall, spiral rainbands, the radius of maximum winds (RMW), ERC scenarios, and other inner-core features. Zhu et al. (2004) show, using the finest grid size of 4 km, that the ERC of Bonnie (1998), accounting for its pronounced intensity changes, occurs as it moves from a strong to a weak VWS environment.

Despite the above-mentioned encouraging achievements, the previous studies also indicate that using cloud-permitting models and simply increasing the horizontal grid resolution do not always lead to a successful simulation of hurricanes (e.g., Davis et al. 2010). Numerical simulation of hurricanes depends on the model representation of various cloud microphysical processes (Zhu and Zhang 2006a; Li and Pu 2008; Davis and Bosart 2002), the planetary boundary layer (PBL) parameterizations (Braun and Tao 2000), vertical resolution (Zhang and Wang 2003; Kimball and Dougherty 2006), and the initial vortex structures (Zhu et al. 2002). Some physics parameterizations appear to depend on grid resolutions and coupling with other schemes. In addition, some real-data simulations have also shown complicated scale interactions involved in hurricane intensity changes (Liu et al. 1999; Hogsett and Zhang 2009).

While the predictability of hurricane intensity change is limited, it is even more challenging to predict the rapid intensification (RI) of hurricanes, where RI is defined as a deepening rate of greater than 1.5 hPa h^{-1} in the minimum central pressure (P_{MIN}) or 15 m s^{-1} per day in the surface maximum tangential wind (V_{MAX}) (Kaplan and DeMaria 2003). So far, the subject of RI has mostly been discussed from the perspective of environmental factors owing to the lack of high-resolution data in the inner-core regions of these storms. Previous studies indicate that warm SST, high relative humidity, and lower VWS are the most favorable environmental factors for RI hurricanes. Kaplan and DeMaria (2003) suggest that a hurricane tends to have the greatest chance of undergoing RI when it is far from its maximum potential intensity (Emanuel 1986) in a favorable environment. Recently, Rogers (2010) demonstrated the ability of a cloud-permitting model to reproduce the RI (at a rate of about 0.8 hPa h^{-1} and 15 m s^{-1} day^{-1}) of Hurricane Dennis (2005) with the finest grid size of 1.667 km.

In contrast to RI, the ERC has received more attention during the past few decades. Since Fortner (1958) first described this phenomenon within Typhoon Sara (1956), a number of observational studies have shown that during the development of some intense hurricanes spiral rainbands may form a second eyewall surrounding an inner eyewall. As the outer eyewall contracts and consolidates, the inner one starts to dissipate. As a result, the hurricane stops intensifying and begins to weaken with rising P_{MIN} and decreasing V_{MAX}. Some time later, the outer eyewall replaces the inner one and becomes the new primary eyewall. After an eyewall succession, the hurricane may resume intensification if conditions are still favorable. Nevertheless, the mechanism by which double eyewalls form still remains elusive due to the lack of high-resolution data, and predicting their occurrences in an operational setting is still a very challenging task.

Therefore, it is the intention of this study to fill in the gaps required to provide a better understanding and aid in the prediction of the RI and ERC processes through a 72-h (0000 UTC 18 October–0000 UTC 21 October 2005) numerical investigation of Hurricane Wilma (2005), a storm that demonstrated record-breaking RI, maximum intensity, and small eye size. In particular, the Geophysical Fluid Dynamics Laboratory's (GFDL) then-operational model, and several other hurricane models, severely underestimated the peak intensity and RI rate of

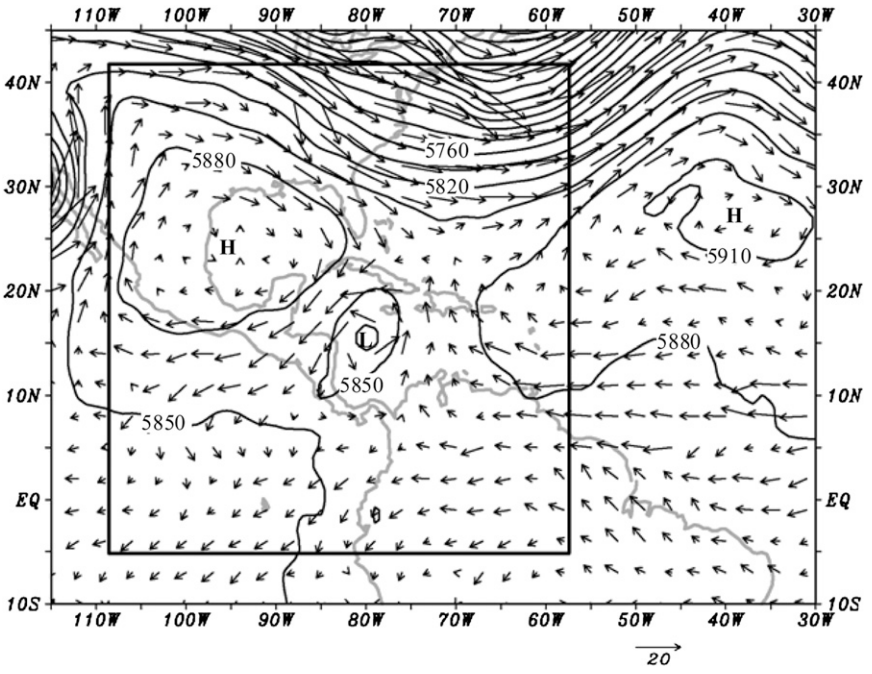

FIG. 1. Horizontal distribution of geopotential height, at intervals of 30 m, superimposed with horizontal flow vectors at 500 hPa from the NCEP GFS analysis at 0000 UTC 18 Oct 2005. The inner frame shows the outermost model domain used for the present study.

Wilma. To establish the credibility of the results of diagnostic and sensitivity simulations to be presented in subsequent parts of this series of papers, the purposes of Part I are to (i) document the life cycle of Hurricane Wilma from its genesis to final dissipation after passing the Florida Peninsula, and some inner-core structures during its RI stage; (ii) examine to what extent Wilma's RI could be predicted using the then-operational GFDL model's initial and lateral boundary conditions but different configurations with the Weather Research and Forecast Model (WRF); and (iii) demonstrate that some inner-core structures (e.g., small eye size, ERCs) in relation to the record-breaking RI and intensity changes could be predicted when a high-resolution cloud-permitting model is used.

The next section provides a brief overview of Hurricane Wilma (2005). Section 3 describes the model configurations used for the prediction of Wilma, as compared to the then-operational GFDL model configurations. Section 4 presents verification of the model-predicted storm structures against various observations. Section 5 shows some model-predicted inner-core structures and structural changes during Wilma's RI stage in order to facilitate the presentation of our model results in the subsequent parts of this series of papers. A summary and some concluding remarks are given in the final section.

2. Overview

Hurricane Wilma (2005) was the most powerful hurricane ever recorded over the Atlantic basin, with a P_{MIN} of 882 hPa and a V_{MAX} that was larger than 80 m s^{-1}, as well as the record-breaking deepening rates of 9.0 hPa h^{-1}, or 54 hPa $(6\ h)^{-1}$, or 83 hPa $(12\ h)^{-1}$ during its 18-h RI phase. The National Centers for Environmental Prediction–National Center for Atmospheric Research (NCEP–NCAR) reanalysis and satellite imagery indicate that the formation of Wilma can be traced back to a broad monsoonlike low-tropospheric trough in the northwestern Caribbean Sea as early as 0000 UTC 11 October. This trough was later split into two parts: the eastern portion moved northeastward and merged with an extratropical cyclone, while the southern portion stayed and grew into a tropical depression (TD) offshore of Jamaica by 1800 UTC 15 October when a concentrated area of deep convection developed on its southeastern side.

Figure 1 shows the representative large-scale environment in which this TD was embedded during the subsequent few days. That is, in the midtroposphere the TD area was sandwiched between a subtropical high to its northwest (hereafter referred to as the Mexican high) and the Atlantic high to its east. This produced a weak steering current, driving the TD slowly west- to west-southwestward

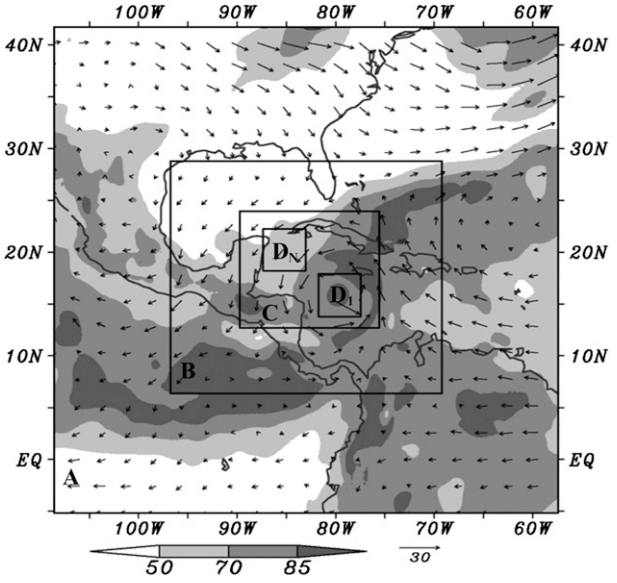

FIG. 2. Model domain configurations, superimposed with surface wind vectors and 600–900-hPa layer-averaged relative humidity (shaded) at 0000 UTC 18 Oct 2005. Domains A, B, C, and D have horizontal resolutions of 27, 9, 3, and 1 km, respectively. Domain D is designed to follow the movement of the storm, with D_1 and D_N denoting its respective initial and final positions.

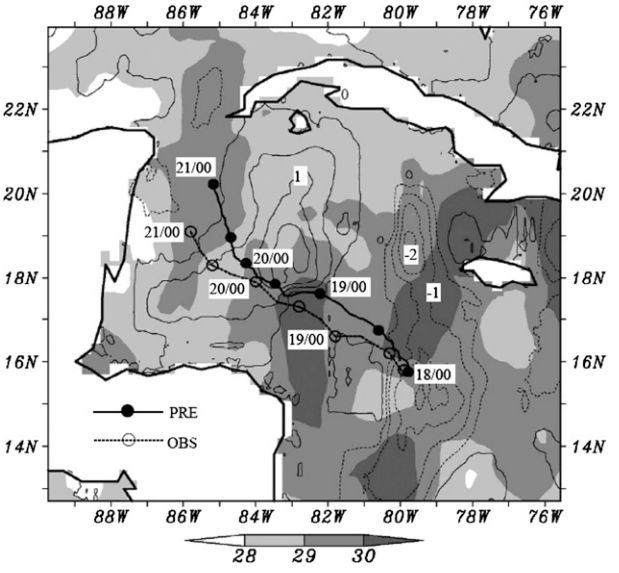

FIG. 3. Comparison of the model-predicted (PRE, thick solid) track of Wilma to the observed track (OBS, thick dashed) over a subdomain during the 72-h period of 0000 UTC 18 Oct–0000 UTC 21 Oct 2005. Shadings show SSTs at the model initial time with thin-solid (for positive values) and thin-dashed lines (for negative values) denoting the SST differences (at intervals of 0.5°C) (i.e., SST at 0000 UTC 19 Oct 2005 minus SST at 0000 UTC 18 Oct 2005).

for about a day and then southwest- to southward for another two days. During this period, convective clouds within the TD were slowly organized with the low-level southwesterly moisture supply from the intertropical convergence zone (ITCZ), but under the influence of a dry-air intrusion in the north-northeasterly flow, as indicated by a dry slot over the Gulf of Mexico, and in the easterly flow (Fig. 2). Around 0600 UTC 17 October, the TD was upgraded to Tropical Storm (TS) Wilma as an intense convective burst occurred on the southern side of the cyclonic circulation where an ample moisture supply was present. It strengthened to hurricane intensity early on 18 October as it turned west-northwestward (Figs. 3 and 4).

Starting from 1800 UTC 18 October, an explosive deepening (RI) episode began when Wilma traversed an area of high ocean heat content. This RI period was sustained for 12 h until 0600 UTC 19 October, with a 29-hPa drop in the first 6 h and a 54-hPa drop in the second 6 h (Fig. 4). Of interest is that corresponding to the respective 29 and 54 hPa $(6\ \text{h})^{-1}$ drops in P_{MIN} are a 10 m s^{-1} increase in V_{MAX} during the first 6 h but only a 5 m s^{-1} increase during the second 6-h period. At first, this 54-hPa drop in P_{MIN} does not appear to be consistent with its corresponding 5 m s^{-1} increase in V_{MAX}, as compared to the pressure–wind relation during the first 6-h RI period. Recently, Kieu et al. (2010) developed a new pressure–wind relationship, based on the analytical model of Kieu and Zhang (2009), and then tested it using preliminary model-predicted data from Hurricane Wilma (2005). Their work indicates that P_{MIN} drops at a rate much faster than the square of V_{MAX}. In particular, when the eye size becomes very small, a slight contraction of the RMW can lead to a large drop in P_{MIN} but small increases in V_{MAX} due to the presence of stronger frictional effects [see Eq. (8) in Kieu et al. (2010)]. Apparently, the pronounced increase of V_{MAX} in the first 6 h could be attributed to the rapid eyewall contraction, based on the conservation of angular momentum, whereas the increased frictional effects or radial winds in the small-sized eyewall region could account for the relatively small increases in V_{MAX} but the more dramatic P_{MIN} drops during the second 6 h.

During the 12-h RI period, a U.S. Air Force reconnaissance flight indicated that the hurricane eye did contract to a very small size, that is, about 4 km in diameter, which is the smallest eye known to the staff of the National Hurricane Center (Pasch et al. 2006). The storm reached its peak intensity at 1200 UTC 19 October with an estimated P_{MIN} of 882 hPa (Fig. 4), which broke the record of 888 hPa set by Hurricane Gilbert (1988) in the Atlantic basin. During the following 24 h, Wilma weakened from 882 to 910 hPa. Satellite imagery reveals that an ERC accounts for this weakening, which replaces

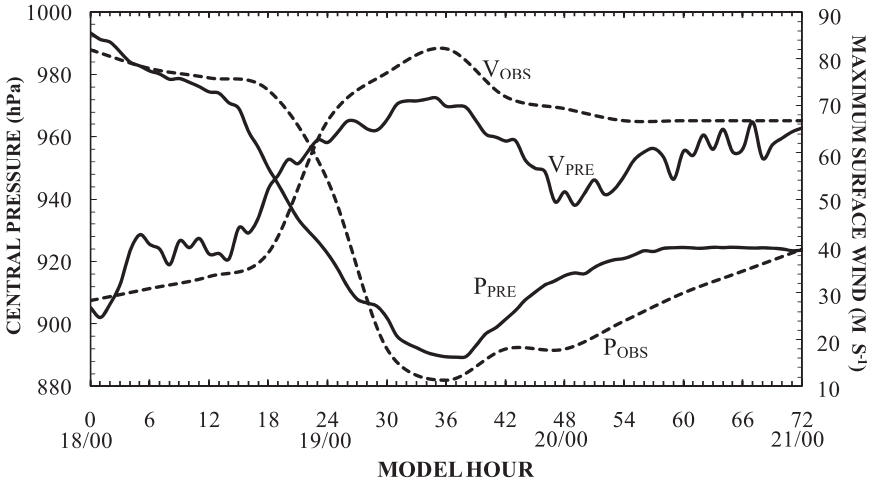

FIG. 4. Time series of model-predicted (PRE, solid) and the observed (OBS, dashed) maximum surface wind (V_{MAX}, m s^{-1}) and minimum sea level pressure (P_{MIN}, hPa) for the period from 18/00-00 to 21/00-72.

the original pinhole eye with a larger one of about 70 km in diameter. A second ERC occurred near the landfalls at Cozumel Island and the northern tip of the Yucatan Peninsula. As a result, Wilma weakened further from 910 to 960 hPa during this 60-h period. After meandering over the northern tip of the Yucatan Peninsula for about a day, Wilma turned north and emerged into the southern Gulf of Mexico around 0000 UTC 23 October, with a V_{MAX} of 43 m s^{-1}. Later on, the storm reintensified over the southeastern Gulf of Mexico when it moved northeastward across a warm ring, and made a third landfall at southwestern Florida near Cape Romano around 1030 UTC 24 October. See Pasch et al. (2006) for more details.

In the present study, we will focus more on the predictability of the record-breaking RI and P_{MIN}, the formation of various inner-core structures in relation to the record-breaking intensity changes, the small-sized eyewall, and an ERC that occurred during the period of 1800 UTC 18 October–0000 UTC 21 October. The then-operational GFDL model underpredicted the storm with negative mean errors of 9, 11, and 15 m s^{-1} for 24-, 48-, and 72 h forecasts, respectively. Its two best forecasts, initialized at 1800 UTC 17 October and 0000 UTC 18 October, produced a peak intensity of 924 hPa with a peak deepening rate of 2.5 hPa h^{-1}. The above-mentioned inner-core structures could not be generated due to the use of coarse (>8 km) resolutions and parameterized convection. Blanton (2008) has attempted to simulate this storm with the finest grid size of 2 km, but produced a peak intensity of 922 hPa occurring 12 h later than observed, similar to the then-operational GFDL model's forecasts.

3. Model description

In this study, Hurricane Wilma (2005) is explicitly predicted using a two-way interactive, movable, quadruply nested (27/9/3/1 km) grid, nonhydrostatic version of the Advanced Research core of the WRF (ARW, version 3.1.1) with the finest grid resolution of 1 km (see Skamarock et al. 2005). The WRF is initialized at 0000 UTC 18 October 2005, which is about 18 h before the onset of RI, and integrated for 72 h, covering the initial rapid spinup, the RI, and the subsequent weakening period associated with an ERC. The model initial and lateral boundary conditions are interpolated from then-operational GFDL model data, that is, from NCEP's Global Forecast System (GFS) analysis, including a bogus vortex based on Kurihara et al.'s (1993) vortex specification scheme. SST is interpolated from the National Oceanic and Atmospheric Administration's (NOAA) Advanced Very High Resolution Radiometer (AVHRR) SST data at 0.25° resolution at 0000 UTC 18 October, and it is held constant in time (see Fig. 3). The time-independent SST is used because of the small changes observed along the storm's track during the RI period. Of interest is that SST became warmer, rather than colder (Leipper 1967; Bender et al. 1993; Zhu and Zhang 2006b), to the right of the track after passing the peak intensity (see the SST differences contoured in Fig. 3). It is evident that the SST in the range of 29°–30°C along the track provides favorable conditions, through the air–sea interaction, for the generation of such an intense hurricane.

Figure 2 shows the quadruply nested WRF domains with Mercator's map projection. Three stationary outer

domains—A, B, and C—have (x, y) dimensions of 200 × 200, 322 × 277, and 496 × 415 grid points with grid spacings of 27, 9, and 3 km, respectively, while a moving innermost domain D with (x, y) dimensions of 451 × 451 and 1-km grid length is used to follow the center of Wilma at 6-min intervals. All of the four domains are activated at the same time: 0000 UTC 18 October. Note that the outermost domain, A, given in Figs. 1 and 2, is the largest domain size, with a Mercator map projection one can obtain from the GFDL data. It covers most of the Mexican high, the western portion of the Atlantic high, the ITCZ to the south, and a midlatitude trough to the north (Fig. 1). All of the domains use 55 σ levels[1] in the vertical, with the model top set at 30 hPa.

The model physics options used include (i) the Thompson et al. (2004) cloud microphysics scheme, which contains six classes of water substance (i.e., water vapor, cloud water, rain, snow, graupel, and cloud ice); (ii) the Yonsei University PBL parameterization with the Monin–Obukhov surface layer scheme (Hong et al. 2006); (iii) the Rapid Radiative Transfer Model (RRTM) for long waves with six molecular species (Mlawer et al. 1997) and the Dudhia (1989) shortwave radiation scheme; and (iv) the Betts–Miller–Janjić (Betts 1986; Betts and Miller 1986; Janjić 1994) cumulus parameterization scheme only for the outermost domain.

We found in our initial experimentation that the following model options are important for the reasonable prediction of the record-breaking intensity and RI rates of Wilma as well as the associated inner-core structures: (i) the finest 1-km horizontal resolution; (ii) the high (55 level) vertical resolution, especially in both the lower and upper tropospheres; and (iii) a cloud-permitting microphysics scheme.

4. Model verification

In this section, we verify the 72-h prediction of Wilma against some selected observations in order to demonstrate the performance of the WRF in predicting the track, intensity, and inner-core structures of the storm using the then-operational data. For this purpose, we compare first the model-predicted track of Wilma to the best-track analysis (see Fig. 3). It is evident that the WRF reproduces the general northwestward movement, which is determined by the large-scale flows associated with the Atlantic high. However, the predicated storm tends to move too fast to the right of the observed during the initial 24 h, causing a final position error of about 120 km that is too far to the north-northeast of the best track. The initial fast movement appears to be attributable to the GFDL bogusing scheme in which a vortex circulation with a radius of greater than 500 km was readjusted (not shown), based on the procedures described by Kurihara et al. (1993). Thus, the mesoscale flow field was somewhat altered. In addition, we find that the model underpredicts the Mexican high to the west of the storm. This implies the generation of weaker northerly flows that accounts partly for the north-northeastward bias of the predicated track.

The time series of the predicted hurricane intensity in terms of P_{MIN} and V_{MAX} are compared to the observed in Fig. 4, showing that despite some differences in the detailed intensity changes the model predicts reasonably well the initial rapid spinup, followed by a period of 18–21-h RI and a subsequent weakening stage, with the final intensity (i.e., at 72 h into the integration, valid at 0000 UTC 21 October, hereafter 21/00-72) that is almost identical to the observed. Although the WRF starts the RI stage 3 h earlier, the predicted strongest intensities are 889 hPa and 72 m s^{-1}, which are 7 hPa and 10 m s^{-1} weaker than the observed P_{MIN} and V_{MAX}, respectively. This yields a mean predicted RI rate of 4 hPa h^{-1} (and 1.6 m s^{-1} h^{-1}), as compared to the observed mean RI rate of 5.2 hPa h^{-1} (and 2.4 m s^{-1} h^{-1}) during the period of 18/18-18 to19/12-36; the peak hourly RI rates from the model prediction and best track are 7 and 9 hPa h^{-1} near 19/06-30, respectively. As will be shown later, this weaker-than-observed storm appears to be caused by a temporal halt of RI between 19/03-27 and 19/05-29, which results from a seemingly fictitious eyewall-merging scenario, and the underpredicted V_{MAX} could be attributed partly to a relatively larger storm size than is observed. Note, however, that Wilma's intensity at 1200 UTC 19 October was extrapolated in time from the dropwindsonde-observed P_{MIN} of 892 hPa and flight-level estimated V_{MAX} of 75 m s^{-1} near 0800 UTC, based on the observation that the storm's central pressure was still falling at this flight time (Pasch et al. 2006).

One may note that the predicted V_{MAX} increases from 52 m s^{-1} at 20/00-48 to 61 m s^{-1} at 20/09-57, while the best track exhibits slow weakening of the storm after reaching its peak intensity. This scenario occurs during the period V_{MAX} at the outer RMW begins to exceed that at the inner RMW, and its subsequent increase results from the contraction of the outer eyewall. Clearly,

[1] The 55 σ levels are given as follows: 1, 0.997, 0.993998, 0.990703, 0.987069, 0.983042, 0.978562, 0.973559, 0.967947, 0.961631, 0.954496, 0.946408, 0.937207, 0.926704, 0.914673, 0.900841, 0.884878, 0.866379, 0.844843, 0.81964, 0.79164, 0.76114, 0.72904, 0.69584, 0.66224, 0.62844, 0.59464, 0.56084, 0.52704, 0.49324, 0.45944, 0.42564, 0.39184, 0.35804, 0.32424, 0.29064, 0.25744, 0.22534, 0.194840, 0.16684, 0.141638, 0.120102, 0.101603, 0.08564, 0.071808, 0.059777, 0.049274, 0.040073, 0.031985, 0.02485, 0.018534, 0.012922, 0.007918, 0.003439, and 0.

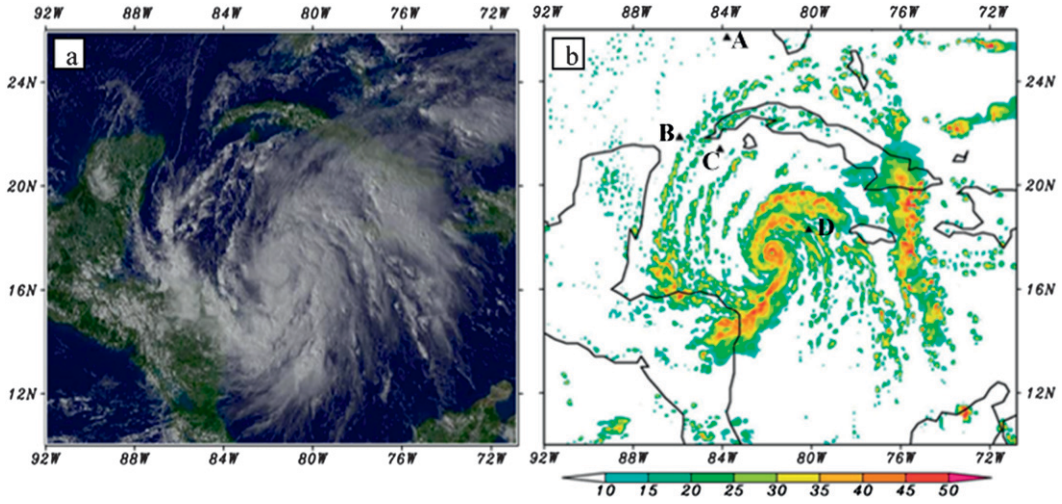

FIG. 5. (a) Visible satellite imagery at 1900 UTC 18 Oct and (b) model-predicted radar reflectivity at $z = 1$ km from the 18-h simulation, valid at 1800 UTC 18 Oct. Letters A, B, C, and D denote the locations of the soundings shown in Fig. 6.

the two RMWs could not be resolved from dropwindsonde observations over Wilma's inner-core region. One may also note that the predicted P_{MIN} increases at a rate larger than that in the best track after 19/18-42. We attribute this more rapid weakening partly to the time-independent SST used that is about 1°–1.5°C colder than the observed to the right of the storm track (i.e., north of 17.5°N; see Fig. 3). In other words, the observed slow weakening of Hurricane Wilma (2005) during its ERC might be related to its movement over the warm-ring region.

Figures 5a and 5b compare the predicted radar reflectivity to a satellite visible image at 1900 UTC 18 October, when the storms just begin their RI stages. Although the two maps show different cloud microphysics variables (i.e., clouds versus precipitation), we can still see that the model reproduces two spiral rainbands to the immediate northeast of the storm, an extensive rainband that wraps around the eyewall starting from the Bahamas, and some scattered convective systems over southern Mexico. It is evident from Fig. 5b that Wilma has spun up to an intense hurricane with a small-sized eyewall, as indicated by a pinhole, which is surrounded by several spiral rainbands within a radius of over 600 km. The inner rainbands will be wrapped around to form an outer eyewall during the next 18 h.

Since the larger-scale flows play an important role in determining the track and intensity as well as the inner-core structures of a hurricane, it is desirable to examine how well the model can reproduce the right prestorm environmental conditions. So, Fig. 6 compares four selected soundings near the onset of RI. They are all taken in the northwest quadrant of the storm (see Fig. 5b for their locations) where the dry air, which appears to affect the distribution of the spiral rainbands and the intensity of Wilma, is likely to have originated, based on satellite imagery (Fig. 5a) and the GFS analysis (see Fig. 2). Two soundings (i.e., A and B) are situated in the vicinity of the outer rainbands, and the other two are located close to the inner-core region (Fig. 5b). Indeed, both the observed and predicted soundings at site A show the presence of an intense inversion layer between 850 and 900 hPa, with a deep dry layer above, due to the influence of the Mexican high. Note the development of a well-mixed, moist PBL in the lowest 100 hPa that represents an important moisture reservoir for storm development over the Gulf of Mexico (where Wilma will move into during the next few days). Comparing to site A, the influence of the Mexican high is much reduced toward site B, as indicated by a much weaker inversion layer and possibly less subsidence-induced drying in the lower troposphere. The observed sounding shows a very moist area in the 800–700-hPa layer, suggesting that the dropwindsonde might have gone through a cloud layer in the outer region (see Fig. 5b).

In contrast, the two soundings taken close to the inner-core regions exhibit moist columns with a near-moist-adiabatic lapse rate up to 300 hPa. This is especially notable at site D, which is located near a major rainband to the north of the storm. Such moist vertical columns are present at most sites in the southern semicircle (not shown), which are closely related to the ITCZ (Fig. 2). Thus, Wilma developed in a rather moist environment with high SST, except for that over the Gulf of Mexico region. The WRF reproduces reasonably well these environmental conditions, as shown in Figs. 5 and 6.

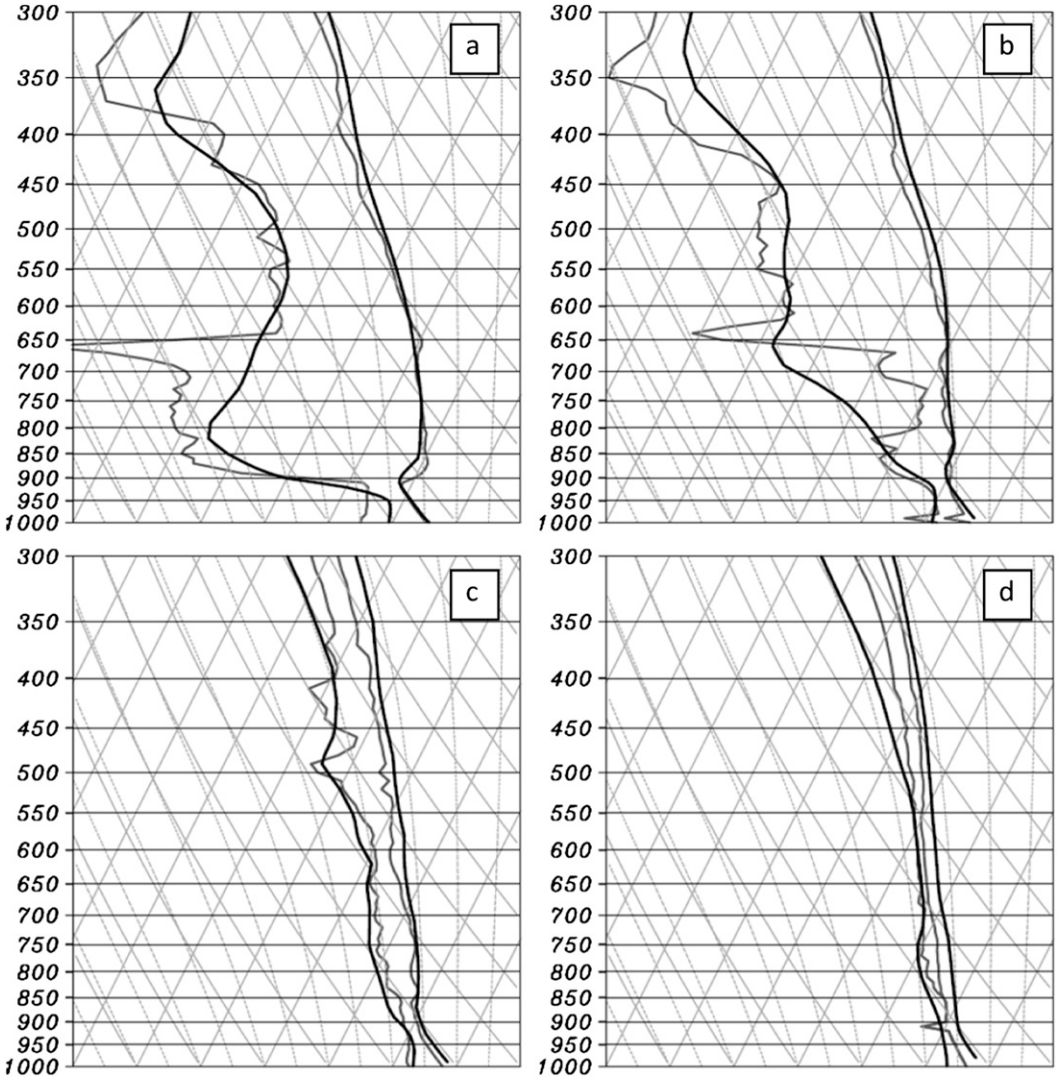

FIG. 6. Comparison of skew T–log p diagrams of soundings taken at points (a) A, (b) B, (c) C, and (d) D, as given in Fig. 5b, between the model prediction (dark black) and the observation (gray) near 1800 UTC 18 Oct.

After verifying the model-predicted larger-scale conditions, we next examine to what extent WRF could reproduce the observed inner-core structures of Wilma. Because observed radar reflectivity maps are not available, we use the 85-GHz satellite images to validate the model-predicted reflectivity near the peak intensity time and at a later weakening stage (see Fig. 7). As we know, cirrus canopies covering TSs in visible and infrared images are transparent at 85 GHz, so these images may be treated as ''the poor man's radar'' for the distribution of deep convection. However, such satellite images are of too-coarse resolution to resolve Wilma's small pinhole eye (i.e., less than 5 km in diameter), and only a small area of intense convection near the center of two large spiral rainbands (A and B) could be seen, presumably as Wilma's inner eyewall (Fig. 7a). Of importance is that the two spiral rainbands were about to be merged to form an outer eyewall, with a wide moat annulus between the two eyewalls at this time. This coincided with the immediate weakening of Wilma after reaching its maximum intensity (cf. Figs. 7a and 4). Another rainband (C), extending from A outward and northeastward, persisted throughout the 72-h period. This type of rainband is labeled by Willoughby et al. (1984) as the principal rainband serving as the interface between the inner-core region and the prestorm environment.

A comparison of Figs. 7a and 7b indicates that WRF reproduces the axisymmetric inner eyewall, surrounded by three rainbands, although the predicted inner eyewall size is larger than the observed and the outer eyewall has

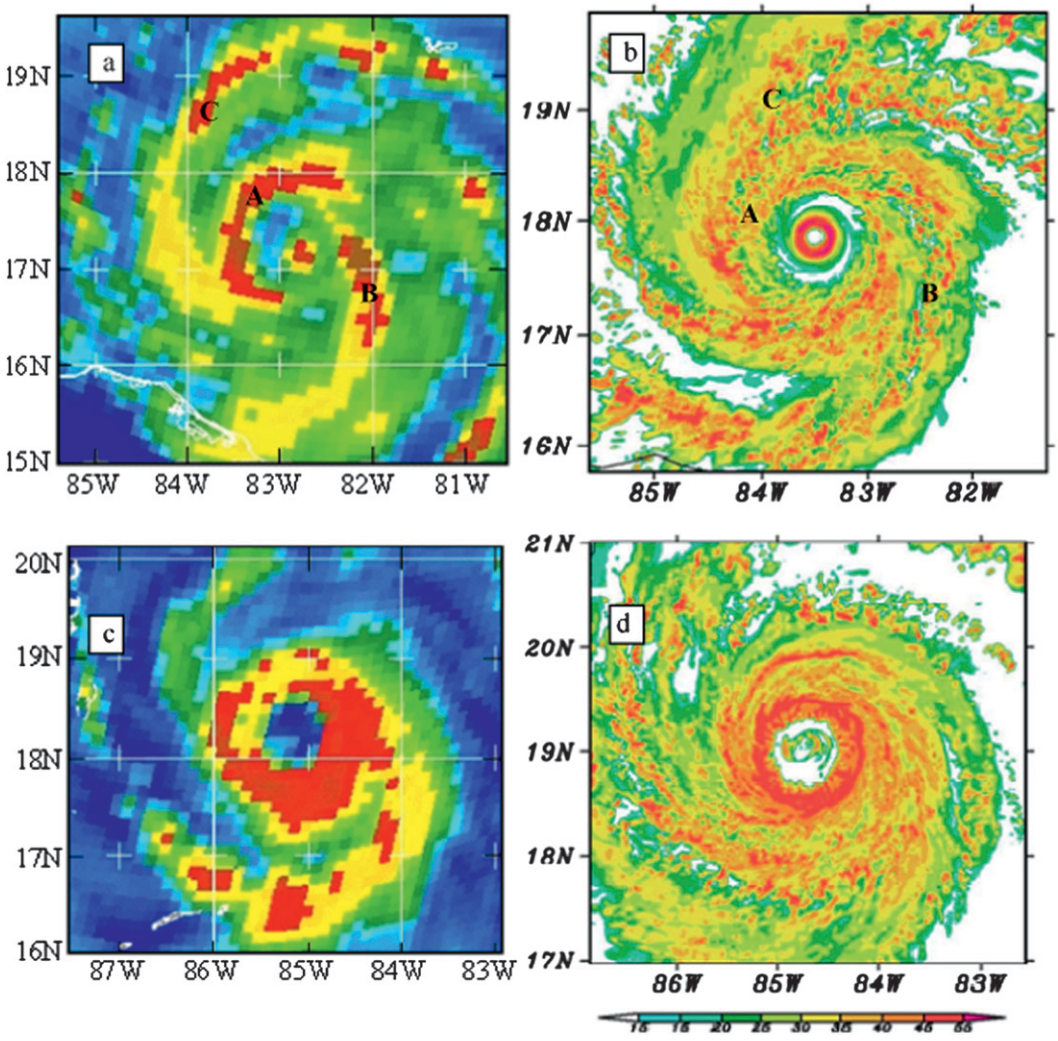

FIG. 7. (a) Special Sensor Microwave Imager (SSM/I) 85-GHz satellite image at 1214 UTC 19 Oct, (b) predicted radar reflectivity over an area of 400 km × 400 km at $z = 1$ km from the 36.25-h forecast (valid at 1215 UTC 19 Oct), and (c) and (d) as in (a) and (b), respectively, but at 1235 UTC 20 Oct and for the 60.5-h forecast (valid at 1230 UTC 20 Oct).

formed from rainbands A and B. The model reproduces the wide coverage of banded convective rainfall in the southern and northern quadrants. Of importance is that the model captures the timing of the outer eyewall formation, which coincides with the weakening of Wilma after reaching its peak intensity. A detailed analysis of the model-predicted radar reflectivity reveals that rainbands B and C form in the inner-core region. As they propagate cyclonically outward, convective cells tend to diminish in their tails because of dry-air intrusion, but are replenished by those outward-propagating cells. Various hypotheses for the propagation of the spiral rainbands and the formation of the outer eyewall have been proposed, such as internal gravity waves (Yamamoto 1963; Kurihara 1976; Elsberry et al. 1987), vortex Rossby waves (MacDonald 1968; Guinn and Schubert 1993; Montgomery and Kallenbach 1997), and recently the mixed vortex-Rossby–inertia/gravity waves (Zhong et al. 2009). These hypotheses will be examined in a future study using the high-resolution model data.

Figures 7c and 7d compare the rainfall structures near 1235 UTC 20 October, which is close to the end of the ERC, as indicated by an eye size of more than 60 km in diameter. The eyewall, newly formed from the closure of the parts of rainbands A and B, was significantly larger in radius and width than the earlier example (cf. Figs. 7c,d and 7a,b). Spiral rainbands were still extended in the northern and southern quadrants during the RI period, except for their varying intensities. That is, the northern (southern) rainband has weakened (intensified),

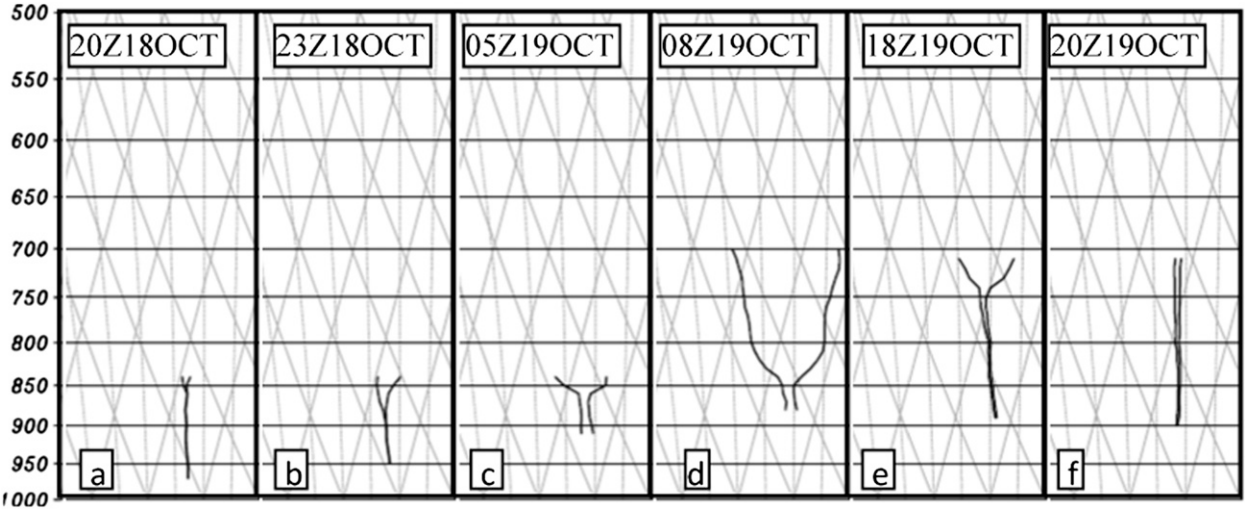

FIG. 8. Skew T–log p diagrams of the soundings taken near the eye center by the U.S. Air Force and NOAA at different stages of the storm.

due likely to the dry (moist) environment in which it was embedded. In general, the model captures the ERC, the more (less) extensive convective rainfall to the south (north), as well as the size and shape of the newly formed eyewall (cf. Figs. 7c and 7d). Note that the satellite data could not resolve the remnants of the inner eyewall as modeled, and appear to have aliased the wide annulus of deep convection outside the outer eyewall as a wide eyewall due to its contamination in sensing rainfall in the lower troposphere.

Figure 8 shows a series of dropwindsondes taken near the eye center by the reconnaissance flight at an altitude of 850 hPa initially (Figs. 8a–c) and later at 700 hPa (Figs. 8d–g). First, we see the PBL depth in the eye decreased from about 150 to 50 hPa during RI, with an intensifying inversion above. According to Zhang and Kieu (2006) the PBL depth in the eye is determined by upward sensible and latent heat fluxes, Ekman pumping, and the compensating subsidence above. In the present case, its upward growth appears to be suppressed by an increase in the subsidence warming and drying from above that was indicative of the RI. This subsidence appears to account for the transformation of an initial saturated to an unsaturated PBL at the later stage of RI (e.g., at 0500 UTC 19 October), with a shallow (~10 hPa) but intense inversion layer below 850 hPa (Fig. 8c). This inversion layer was thickened to about 40 hPa just 3 h later (i.e., 0800 UTC 19 October; see Fig. 8d), namely, shortly after entering a relatively slower RI stage (see Fig. 4). Subsequently, as the storm weakened, the eye PBL grew rapidly from an estimated depth of less than 50 hPa at 0800 UTC 19 October to about 150 hPa at 1800 UTC 19 October (cf. Figs. 8d and 8e) as a result of Ekman pumping overpowering the subsidence drying/warming. Willoughby (1998) has documented a similar scenario in Hurricane Olivia (1994) in which the base of the inversion layer was elevated from 830 to 740 hPa as its P_{MIN} rose from 930 to 937 hPa in 2.7 h.

It is apparent by comparing Figs. 8 and 9 that the model-predicted eye soundings compare favorably to the observed up to 18/23–23. Of interest is that the model predicts three different layers in the eye: a well-mixed but unsaturated layer with the dry-adiabatic lapse rate in the lowest 50 hPa, a saturated layer with the moist-adiabatic lapse rate (but little condensation occurring) above, and a dry and warm air layer with a thermal inversion aloft (Fig. 9). Willoughby (1998) has shown the existence of such a shallow, well-mixed PBL in Hurricane Olivia (1994), although it is not evident in the observed soundings given in Fig. 8. Of primary concern is that the model appears to overpredict the growth of the saturated layer and underpredict the inversion intensity above, especially during the RI period (cf. Figs. 9c,d and 8c,d). This indicates that the predicted dry subsidence warming and drying in the eye may be too weak to compensate for the upward transport of sensible and moisture fluxes by Ekman pumping (see Zhang et al. 2002; Zhang and Kieu 2006). In addition, numerical horizontal diffusion, calculated at constant pressure surfaces, could account for a significant portion of the moistening in the layer (Zhang et al. 2002), when considering the relatively small eye being modeled. As a result, the model overpredicts the depth of the moist layer at 19/20–44 (cf. Figs. 8f and 9f).

Figure 10a shows the radial profiles of tangential winds observed at the flight level. At 2130 UTC 18 October,

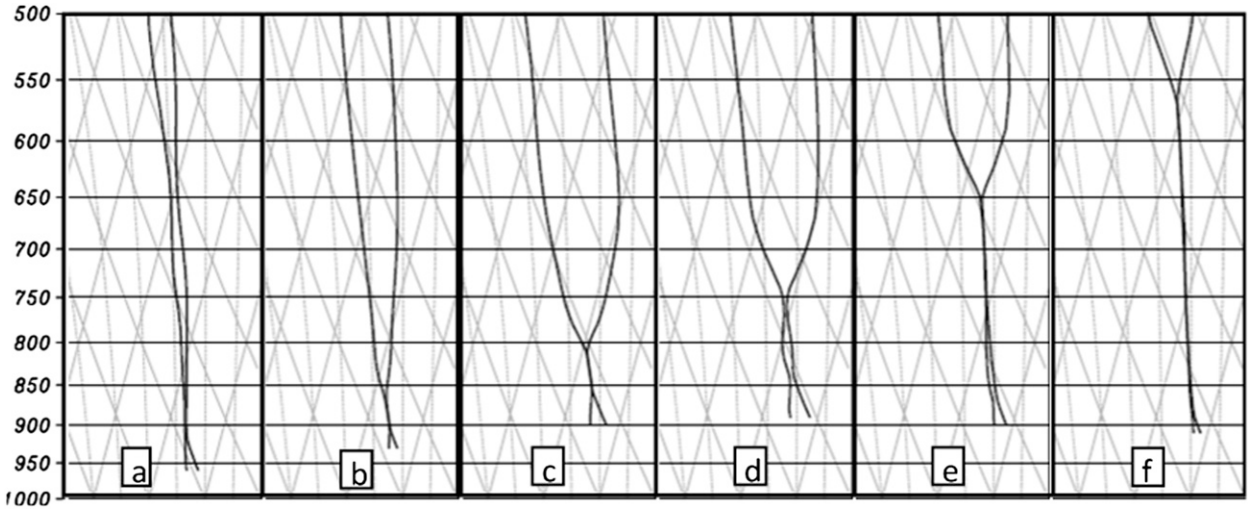

FIG. 9. As in Fig. 8, but from the model prediction.

when Wilma was in its early RI stage, we see a maximum wind of 40 m s^{-1} located at $r = 20$ km, with a relatively flat radial profile beyond $r = 50$ km. In the next available flight-level profile (i.e., by 1800 UTC 19 October), the maximum wind speed had doubled and the RMW had contracted to about 8 km, with a much sharper radial profile than that 20 h earlier. Note that another local wind maximum developed near $r = 60$ km, which was indicative of the development of the outer eyewall. Subsequently, this outer RMW was contracting while the associated peak wind continued to increase. Meanwhile, the inner wind maximum weakened from 80 to 70 m s^{-1} during the period of 1800 UTC 19 October–2140 UTC 19 October. The inner and outer wind maxima reached a comparable strength at 0500 UTC 20 October, with the deepest saddle wind profile and the most pronounced moat area between. Because the contracting outer eyewall choked off the inward energy supply, the inner eyewall dissipated with time. As a result, the inner eyewall/wind maximum disappeared by 2140 UTC 20 October, with the previous pinhole eye and RMW of 8 km replaced by a large eye with an RMW of about 35 km. The increased RMW implies that the efficiency of diabatic heating in intensifying the storm was significantly reduced after the ERC, according to Hack and Schubert (1986).

It is evident that the model predicts reasonably well the formation of an outer RMW/eyewall near the end of RI, the subsequent dissipation (growth) of the inner (outer) eyewall, and the 18–24-h duration of the ERC (cf. Figs. 10a and 10b). However, the inner RMW is predicted to be about twice as large as observed, with a slower-than-observed contraction rate occurring during the RI period (e.g., from 18/1830-18.5 to 19/18-42). It appears that both the larger RMW and the slower contraction could be attributed to the development of an artificial outer eyewall during the period of 19/00–24 to 19/06–30 (see Fig. 11). Similarly, the predicted outer eyewall also contracts more slowly than does the observed, although the model reproduces reasonably well the outer RMW size near the end of RI. We may attribute this to the above-mentioned too large inner eyewall predicted, with less-than-observed radial gradients in tangential wind outward from the inner RMW. As pointed out by Willoughby (1988), the contraction rate is determined by the ratio of the tangential wind increase to its radial gradient evaluated on the inward side of the RMW. In other words, the predicted radial wind profile tends to transport less absolute angular momentum inward than the observed for the amplification of rotation at the outer RMW, causing relatively weaker rotational winds in the outer region.

In summary, the model predicts reasonably well the track and intensity of Hurricane Wilma (2005), including its RI, the eye's thermal structures, double eyewalls, and the moat area between as well as the ERC. In spite of some discrepancies in the detailed structures, the general agreement between the model prediction and the observations will allow us to use the model results in the next section to examine various inner-core structures associated with the RI and intensity changes of Wilma.

5. Model-predicted structural changes

It has been recently realized that the RI and intensity changes are often associated with the rapid eyewall contraction, the ERC, and some inner-core structural changes (e.g., Willoughby et al. 1982; Zhu et al. 2004; Lee and Bell 2007; Rogers 2010). For this purpose, Fig. 11

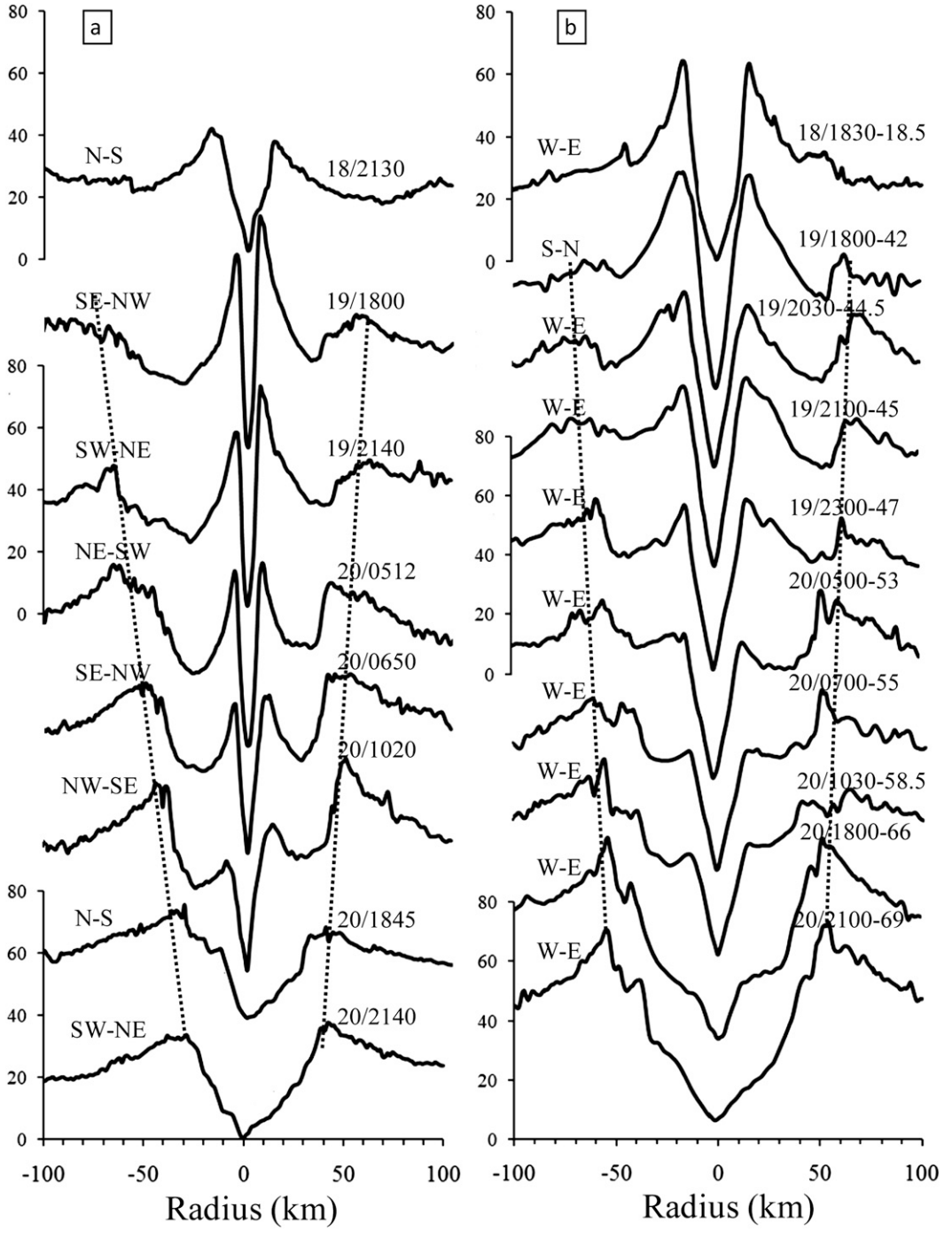

FIG. 10. Comparison of radial profiles of flight-level tangential winds spanning a diameter of 200 km within Wilma: (a) observations and (b) model prediction. Dashed lines indicate the evolution of the RMW.

shows the radius–time cross section of tangential winds and radar reflectivity (at $z = 3$ km) during the 72-h integration period. At the model initial time, deep convection is highly asymmetrically distributed in Wilma's eyewall due to the presence of moderate vertical wind shear (not shown), and the hurricane vortex has an RMW of about 70–80 km. The RMW decreases rapidly to 30 km during the initial 12-h rapid spinup (cf. Figs. 11 and 4). Such a rapid decrease in RMW has also been observed in the other RI storms, for example, Elena of 1985 (see Corbosiero et al. 2005) and Gabrielle of 2001 (Molinari and Vollaro 2010). This rapid contraction

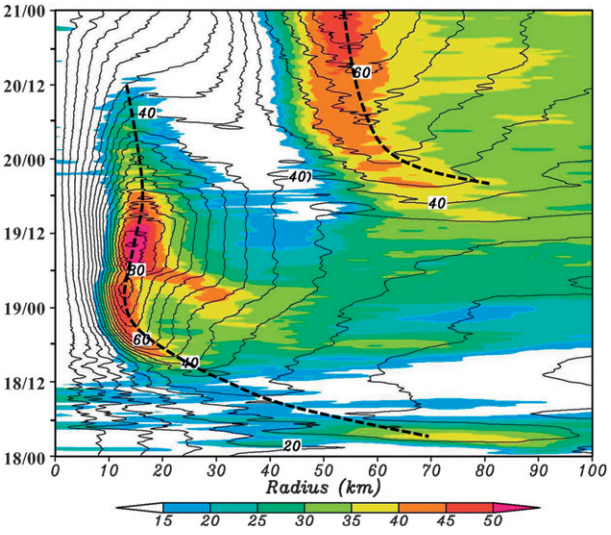

FIG. 11. Tangential winds as a function of time and radial distance (every 5 m s^{-1}), superimposed with the radar reflectivity (dBZ), at $z = 3$ km from the 72-h model integration between 18/00-00 and 21/00-72. Dashed lines denote the RMW.

may result from the development of convective bursts, which has been the subject of numerous observational and model studies (e.g., Heymsfield et al. 2001; Kelley et al. 2004; Squires and Businger 2008; Reasor et al. 2009; Guimond et al. 2010; Rogers 2010). This subject will be explored in Part II of this series of papers.

The model-predicted radar reflectivity shows the closure of the eyewall near 18/15-15, coinciding with the onset of Wilma's RI, although the convective asymmetry is still evident, with an irregular eyewall (see Fig. 12a). The RMW and eyewall continue to contract and become more axisymmetric and robust, reaching the smallest RMW of 12 km (at $z = 1$ km) at 19/03-27, which is consistent with the continuous RI (cf. Figs. 4 and 12e). Meanwhile, three to four spiral rainbands within a radial interval of 20–30 km begin to merge and form a secondary eyewall at 18/21-21 (Fig. 12c), and this eyewall contracts at a rate much faster than the inner eyewall shortly after. Because of the different contracting rates, the two eyewalls merge between 19/03-27 and 19/5-29 and form a wide eyewall, shifting both the updraft core and RMW slightly outward (cf. Figs. 12e,f and 11). As a result, Wilma's RI is temporally halted during this 2-h period (see Fig. 4). Note that the inner eyewall exhibits little evidence of dissipation while the secondary eyewall contracts (cf. Figs. 11 and 12c–e). In this regard, the merging process differs from the ERC. Although this merging scenario is not supported by the observed intensity changes in Wilma, it may appear in other hurricanes when an outer eyewall is formed close to an inner eyewall (i.e., with a narrow moat area). In the present case, we attribute the merged eyewall to the use of Thompson et al.'s (2004) cloud microphysics scheme, because it is absent when the other microphysics schemes are used.

The modeled storm resumes its RI after 19/05-29 with the peak RI rate of about 7 hPa h^{-1} from 19/06-30 to 19/07-31, and reaches its peak intensity near 19/12-36 as observed (Fig. 4). However, the RMW and eyewall do not contract during the final 6-h RI stage (Fig. 11). The storm begins to weaken as another eyewall forms near the radius of 65 km and the inner eyewall dissipates (Fig. 13). This scenario fits well the typical ERC as described in section 1. Of significance is that unlike those short-lived [e.g., Andrew of 1992 (Liu et al. 1997); Bonnie of 1998 (Rogers et al. 2003; Zhu et al. 2004)], this ERC lasts for as long as 24 h from both the model and observations (see Figs. 13 and 10). Such a long ERC could be attributed to the development of the large outer RMW with a wide moat area between the inner and outer eyewalls (see Figs. 13 and 14). Specifically, based on the balanced dynamics of Kieu and Zhang (2010), the outer eyewall tends to generate inside itself a deep layer of anticyclonic flow to offset the cyclonic rotation of the inner eyewall. It also generates an outward convergent flow in the PBL to block the energy supply to deep convection in the inner eyewall, and subsidence between the two eyewalls to suppress convective development in the inner eyewall. Because of the inertial stability of the inner vortex, these negative effects tend to occur closer to the outer eyewall, as can be seen from the buildup of large radial gradients of the tangential winds near the outer RMW (see Figs. 10 and 11). It appears that warm SST over the region also helps maintain deep convection in the inner eyewall, as indicated by small decreases in equivalent potential temperature (θ_e) in the eye PBL (see Fig. 14). Clearly, the greater the moat area, the longer is the ERC.

Figure 14 also shows the vertical cross-sectional evolution of the ERC in terms of θ_e and vertical circulations. During the early ERC stage, we see strong radial gradients of θ_e in the inner eyewall with a θ_e minimum in the eye and another one between the inner and outer eyewalls (Fig. 14a). The latter eyewall is consistent with the presence of the minimum θ_e at $z = 3$ km in the environment, and is clearly isolated by deep convection transporting high-θ_e air upward in the outer eyewall. By 20/06-54, the inner eyewall has weakened substantially, with decreasing θ_e gradients, while the outer eyewall has fully developed, with a well-defined cloud-free moat area between (Fig. 14b). Some evaporatively driven moist downdrafts can be seen, initially at the outer edge of the inner eyewall, as it is surrounded by dry subsidence.

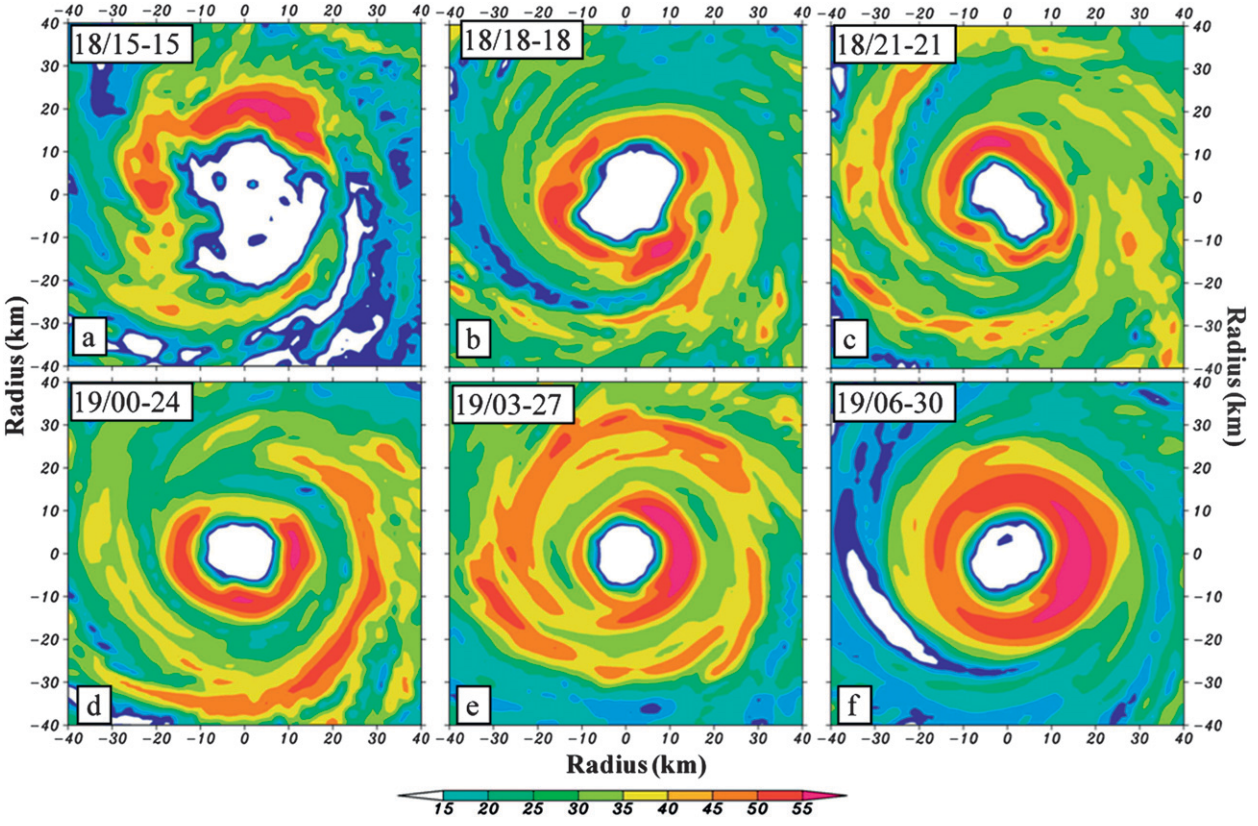

FIG. 12. Predicted radar reflectivity (dBZ) at 3-hourly intervals at $z = 1$ km over a subdomain of 80 km $\times$ 80 km from the 15–30-h model integration between 18/15-15 and 19/06-30.

These moist downdrafts must play an important role in speeding up the collapse of the inner eyewall. Near the end of the ERC, a large-sized eye is developed with little evidence of clouds associated with the inner eyewall. However, the θ_e structures still exhibit the footprint of the inner eyewall, even long after the complete dissipation of the inner eyewall convection. Higher-θ_e air may be expected in the eye resulting from a mixture of the air masses in the original eye, inner eyewall, and moat area. Thus, the ERC can alter significantly the thermodynamical properties in the inner-core region of a hurricane.

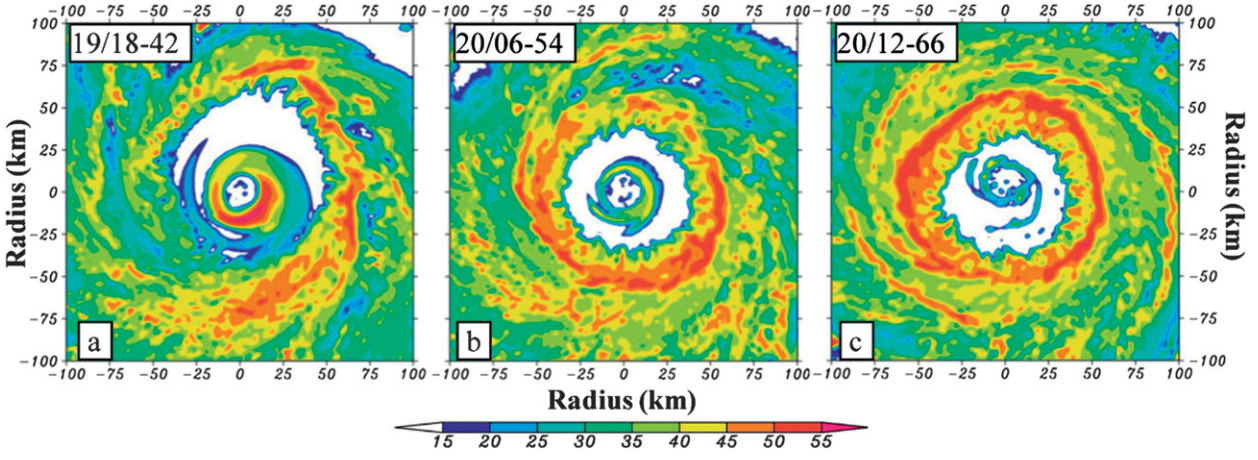

FIG. 13. Predicted radar reflectivity (dBZ) at $z = 1$ km in a subdomain of 200 km $\times$ 200 km at (a)19/18-42, (b) 20/06-54, and (c) 20/18-66.

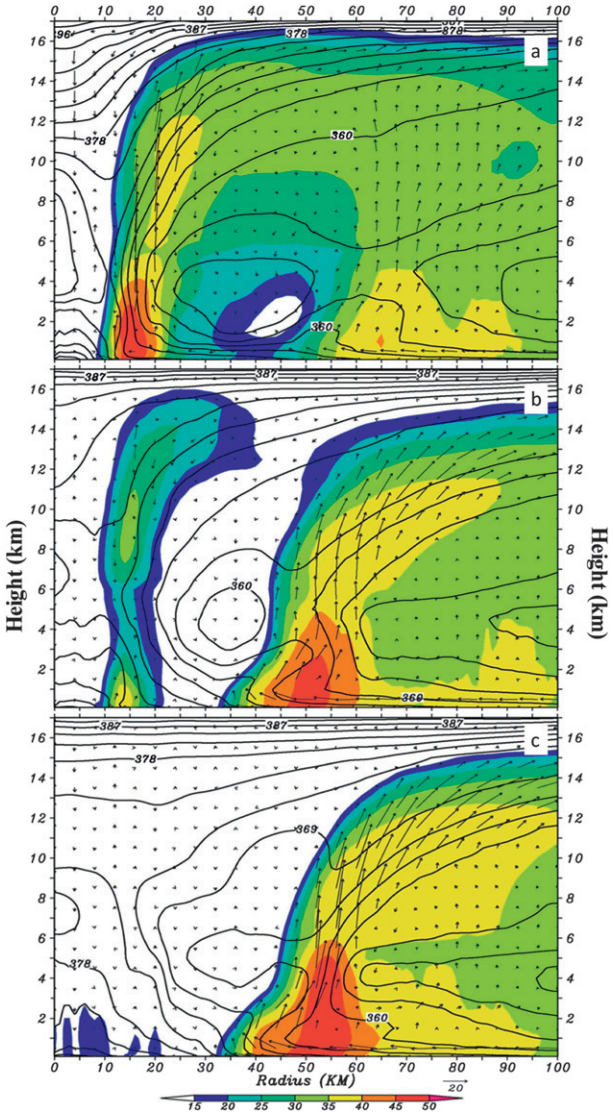

FIG. 14. Azimuthally averaged equivalent potential temperature (θ_e) as a function of radius and height at intervals of 3 K and radar reflectivity (dBZ, shaded), superimposed with in-plane flow vectors, at (a) 19/18-42, (b) 20/06-54, and (c) 20/18-66.

6. Summary and conclusions

In this study, we present a 72-h numerical prediction of the record-breaking development of Hurricane Wilma (2005) using a two-way interactive, movable, multinested-grid (27/9/3/1 km), cloud-permitting version of the WRF-ARW using the initial and boundary conditions that would be available in an operational setting. It is demonstrated that the WRF reproduces reasonably well the track, initial rapid spinup, RI, peak intensity, and subsequent weakening of the storm, as verified against various observations. In particular, the model captures the timing of the occurrence of RI, the peak intensity, and subsequent weakening of Wilma. Specifically, the model predicts a peak intensity of 889 hPa in P_{MIN} and 72 m s^{-1} in V_{MAX}, and a mean deepening rate of more than 4 hPa h^{-1} during an 18-h RI period, as compared to the observed 882 hPa and 82 m s^{-1}, and 5.2 hPa h^{-1} mean RI rates. The model also predicts the peak deepening rate of 7–8 hPa h^{-1}, albeit for about 1 h, near the end of Wilma's final RI stage. However, the onset of RI is predicted 2–3 h earlier than the observed and the model-predicted track is about 120 km too far to the north-northeast of the best track at the end of the 72-h prediction.

Of particular importance is that the model reproduces the basic distribution of spiral rainbands, the timing and duration of the ERC, and the size of the outer eyewall. The model also reproduces reasonably well the suppression of PBL development in the eye with an intense warming and drying above during the RI period, and the rapid growth of the eye PBL with a moist-adiabatic lapse rate during Wilma's weakening stage. In addition, the model-predicted flow fields compare favorably to the flight-level observations, except for the inner RMW, which is twice as large as observed.

It is found through a series of sensitivity simulations that the above-mentioned intensity and structural changes can be more or less predicted with the peak intensity of at least less than 900 hPa when different cloud microphysics and PBL schemes are used in the WRF. This implies that large-scale environmental conditions, including warm SST, play an important role in determining the quality of the model-predicted intensity and structural changes of the storm. Based on these results, we may state that it is possible to improve the forecasts of hurricane intensity and intensity changes, and especially RI, if the inner-core structural changes and right storm size can be reasonably predicted in an operational setting with high-resolution cloud-permitting models, realistic initial conditions, and model physical parameterizations. In the subsequent parts of this series of papers, we will use the model results to help us understand the inner-core dynamics of the RI, ERC, and multiscale interactions involved in the development of Hurricane Wilma. In addition, the sensitivity simulations will be analyzed to gain insights into the relative importance of various parameters in affecting the inner-core structures and patterns of evolution of the storm and in obtaining the reasonable prediction of the features presented herein.

Acknowledgments. We thank Dr. Weixing Shen for his kind assistance in accessing the then-operational GFDL dataset for the current study. The final WRF model integration was completed on NOAA's NJET supercomputer through the Hurricane Forecast Improvement

Program. This work was supported by NASA Grant 1284085, ONR Grant N000140710186, and NSF Grant ATM0758609.

REFERENCES

Bender, M. A., I. Ginis, and Y. Kurihara, 1993: Numerical simulations of tropical cyclone–ocean interaction with a high resolution coupled model. *J. Geophys. Res.,* **98,** 23 245–23 263.

Betts, A. K., 1986: A new convective adjustment scheme. Part I: Observational and theoretical basis. *Quart. J. Roy. Meteor. Soc.,* **112,** 677–691.

——, and M. J. Miller, 1986: A new convective adjustment scheme. Part II: Single column tests using GATE wave, BOMEX, and Arctic air-mass data sets. *Quart. J. Roy. Meteor. Soc.,* **112,** 693–709.

Black, M. L., and H. E. Willoughby, 1992: The concentric eyewall cycle of Hurricane Gilbert. *Mon. Wea. Rev.,* **120,** 947–957.

Blackwell, K. G., 2000: The evolution of Hurricane Danny (1997) at landfall: Doppler-observed eyewall replacement, vortex contraction/intensification, and low-level wind maxima. *Mon. Wea. Rev.,* **128,** 4002–4016.

Blanton, C. E., 2008: Polygonal eyewalls in a 2 km WRF simulation of Wilma (2005). Preprints, *28th Conf. on Hurricanes and Tropical Meteorology,* Orlando, FL, Amer. Meteor. Soc., 7A.6. [Available online at http://ams.confex.com/ams/pdfpapers/138713.pdf.]

Bluestein, H. B., and D. S. Hazen, 1989: Doppler-radar analysis of a tropical cyclone over land: Hurricane Alicia (1983) in Oklahoma. *Mon. Wea. Rev.,* **117,** 2594–2611.

Braun, S. A., 2002: A cloud-resolving simulation of Hurricane Bob (1991): Storm structure and eyewall buoyancy. *Mon. Wea. Rev.,* **130,** 1573–1592.

——, and W. Tao, 2000: Sensitivity of high-resolution simulations of Hurricane Bob (1991) to planetary boundary layer parameterizations. *Mon. Wea. Rev.,* **128,** 3941–3961.

Corbosiero, K. L., J. Molinari, and M. L. Black, 2005: The structure and evolution of Hurricane Elena (1985). Part I: Symmetric intensification. *Mon. Wea. Rev.,* **133,** 2905–2921.

Davis, C. A., and L. F. Bosart, 2001: Numerical simulations of the genesis of Hurricane Diana (1984). Part I: Control simulation. *Mon. Wea. Rev.,* **129,** 1859–1881.

——, and ——, 2002: Numerical simulations of the genesis of Hurricane Diana (1984). Part II: Sensitivity of track and intensity prediction. *Mon. Wea. Rev.,* **130,** 1100–1124.

——, W. Wang, J. Dudhia, and R. Torn, 2010: Does increased horizontal resolution improve hurricane wind forecasts? *Wea. Forecasting,* **25,** 1826–1841.

Dudhia, J., 1989: Numerical study of convection observed during the Winter Monsoon Experiment using a mesoscale two-dimensional model. *J. Atmos. Sci.,* **46,** 3077–3107.

Elsberry, R. L., W. M. Frank, G. J. Holland, J. D. Jarrell, and R. L. Southern, 1987: *A Global View of Tropical Cyclones*. University of Chicago Press, 185 pp.

Emanuel, K. A., 1986: An air–sea interaction theory for tropical cyclones. Part I: Steady-state maintenance. *J. Atmos. Sci.,* **43,** 585–605.

Fortner, L. E., 1958: Typhoon Sarah, 1956. *Bull. Amer. Meteor. Soc.,* **39,** 633–639.

Guimond, S. R., G. M. Heymsfield, and F. J. Turk, 2010: Multiscale observations of Hurricane Dennis (2005): The effects of hot towers on rapid intensification. *J. Atmos. Sci.,* **67,** 633–654.

Guinn, T. A., and W. H. Schubert, 1993: Hurricane spiral bands. *J. Atmos. Sci.,* **50,** 3380–3403.

Hack, J. J., and W. H. Schubert, 1986: Nonlinear response of atmospheric vortices to heating by organized cumulus convection. *J. Atmos. Sci.,* **43,** 1559–1573.

Heymsfield, G. M., J. B. Halverson, J. Simpson, L. Tian, and T. P. Bui, 2001: ER-2 Doppler radar investigations of the eyewall of Hurricane Bonnie during the Convection and Moisture Experiment-3. *J. Appl. Meteor.,* **40,** 1310–1330.

Hogsett, W., and D.-L. Zhang, 2009: Numerical simulation of Hurricane Bonnie (1998). Part III: Energetics. *J. Atmos. Sci.,* **66,** 2678–2696.

Hong, S.-Y., Y. Noh, and J. Dudhia, 2006: A new vertical diffusion package with an explicit treatment of entrainment processes. *Mon. Wea. Rev.,* **134,** 2318–2341.

Janjić, Z. I., 1994: The step-mountain eta coordinate model: Further developments of the convection, viscous sublayer, and turbulence closure schemes. *Mon. Wea. Rev.,* **122,** 927–945.

Kaplan, J., and M. DeMaria, 2003: Large-scale characteristics of rapidly intensifying tropical cyclones in the North Atlantic basin. *Wea. Forecasting,* **18,** 1093–1108.

Kelley, O. A., J. Stout, and J. B. Halverson, 2004: Tall precipitation cells in tropical cyclone eyewalls are associated with tropical cyclone intensification. *Geophys. Res. Lett.,* **31,** L24112, doi:10.1029/2004GL021616.

Kieu, C. Q., and D.-L. Zhang, 2009: An analytical model for the rapid intensification for tropical cyclones. *Quart. J. Roy. Meteor. Soc.,* **135,** 1336–1349.

——, and ——, 2010: A piecewise potential vorticity inversion algorithm and its application to hurricane inner-core anomalies. *J. Atmos. Sci.,* **67,** 2616–2631.

——, H. Chen, and D.-L. Zhang, 2010: An examination of the pressure–wind relationship in intense tropical cyclones. *Wea. Forecasting,* **25,** 895–907.

Kimball, S. K., and F. C. Dougherty, 2006: The sensitivity of idealized hurricane structure and development to the distribution of vertical levels in MM5. *Mon. Wea. Rev.,* **134,** 1987–2008.

Kurihara, Y., 1976: On the development of spiral bands in a tropical cyclone. *J. Atmos. Sci.,* **33,** 940–958.

——, M. A. Bender, and R. J. Ross, 1993: An initialization scheme of hurricane models by vortex specification. *Mon. Wea. Rev.,* **121,** 2030–2045.

Lee, W., and M. M. Bell, 2007: Rapid intensification, eyewall contraction, and breakdown of Hurricane Charley (2004) near landfall. *Geophys. Res. Lett.,* **34,** L02802, doi:10.1029/2006GL027889.

Leipper, D., 1967: Observed ocean conditions and hurricane Hilda, 1964. *J. Atmos. Sci.,* **24,** 182–196.

Li, X., and Z. Pu, 2008: Sensitivity of numerical simulation of early rapid intensification of Hurricane Emily (2005) to cloud microphysical and planetary boundary layer parameterizations. *Mon. Wea. Rev.,* **136,** 4819–4838.

Liu, Y., D.-L. Zhang, and M. K. Yau, 1997: A multiscale numerical study of Hurricane Andrew (1992). Part I: Explicit simulation and verification. *Mon. Wea. Rev.,* **125,** 3073–3093.

——, ——, and ——, 1999: A multiscale numerical study of Hurricane Andrew (1992). Part II: Kinematics and inner-core structures. *Mon. Wea. Rev.,* **127,** 2597–2616.

MacDonald, N. J., 1968: The evidence for the existence of Rossby-like waves in the hurricane vortex. *Tellus,* **20,** 138–150.

Marks, F. D., Jr., and R. A. Houze Jr., 1984: Airborne Doppler radar observations in Hurricane Debby. *Bull. Amer. Meteor. Soc.,* **65,** 569–582.

——, and ——, 1987: Inner core structure of Hurricane Alicia from airborne Doppler radar observations. *J. Atmos. Sci.,* **44,** 1296–1317.

——, and Coauthors, 1998: Landfalling tropical cyclones: Forecast problems and associated research opportunities. Report of the Fifth Prospectus Development Team to the U.S. Weather Research Program. *Bull. Amer. Meteor. Soc.,* **79,** 305–323.

Mlawer, E. J., S. J. Taubman, P. D. Brown, M. J. Iacono, and S. A. Clough, 1997: Radiative transfer for inhomogeneous atmosphere: RRTM, a validated correlated-k model for the longwave. *J. Geophys. Res.,* **102** (D14), 16 663–16 682.

Molinari, J., and D. Vollaro, 2010: Rapid intensification of a sheared tropical storm. *Mon. Wea. Rev.,* **138,** 3869–3885.

Montgomery, M. T., and R. J. Kallenbach, 1997: A theory for vortex Rossby-waves and its application to spiral bands and intensity changes in hurricanes. *Quart. J. Roy. Meteor. Soc.,* **123,** 435–465.

Parrish, J. R., R. W. Burpee, F. D. Marks, and R. Grebe, 1982: Rainfall patterns observed by digitized radar during the landfall of Hurricane Frederic (1979). *Mon. Wea. Rev.,* **110,** 1933–1944.

Pasch, R. J., E. S. Blake, H. D. Cobb III, and D. P. Roberts, 2006: Tropical cyclone report: Hurricane Wilma, 15–25 October 2005. NOAA/NHC, 27 pp. [Available online at http://www.nhc.noaa.gov/pdf/TCR-AL252005_Wilma.pdf.]

Rappaport, E. N., and Coauthors, 2009: Advances and challenges at the National Hurricane Center. *Wea. Forecasting,* **24,** 395–419.

Reasor, P. D., M. D. Eastin, and J. F. Gamache, 2009: Rapidly intensifying Hurricane Guillermo (1997). Part I: Low-wavenumber structure and evolution. *Mon. Wea. Rev.,* **137,** 603–631.

Rogers, R., 2010: Convective-scale structure and evolution during a high-resolution simulation of tropical cyclone rapid intensification. *J. Atmos. Sci.,* **67,** 44–70.

——, S. Chen, J. Tenerelli, and H. E. Willoughby, 2003: A numerical study of the impact of vertical shear on the distribution of rainfall in Hurricane Bonnie (1998). *Mon. Wea. Rev.,* **131,** 1577–1599.

Shen, B.-W., W.-K. Tao, W. K. Lau, and R. Atlas, 2010: Predicting tropical cyclogenesis with a global mesoscale model: Hierarchical multiscale interactions during the formation of Tropical Cyclone Nargis (2008). *J. Geophys. Res.,* **115,** D14102, doi:10.1029/2009JD013140.

Skamarock, W. C., and Coauthors, 2005: A description of the Advanced Research WRF version 3. NCAR Tech. Note 475+STR, 125 pp.

Squires, K., and S. Businger, 2008: The morphology of eyewall lightning outbreaks in two category 5 hurricanes. *Mon. Wea. Rev.,* **136,** 1706–1726.

Thompson, G., R. M. Rasmussen, and K. Manning, 2004: Explicit forecasts of winter precipitation using an improved bulk microphysics scheme. Part I: Description and sensitivity analysis. *Mon. Wea. Rev.,* **132,** 519–542.

Willoughby, H. E., 1988: The dynamics of the tropical cyclone core. *Aust. Meteor. Mag.,* **36,** 183–191.

——, 1998: Tropical cyclone eye thermodynamics. *Mon. Wea. Rev.,* **126,** 3053–3067.

——, J. A. Clos, and M. Shoreibah, 1982: Concentric eye walls, secondary wind maxima, and the evolution of the hurricane vortex. *J. Atmos. Sci.,* **39,** 395–411.

——, F. D. Marks Jr., and R. J. Feinberg, 1984: Stationary and moving convective bands in hurricanes. *J. Atmos. Sci.,* **41,** 3189–3211.

Yamamoto, R., 1963: A dynamical theory of spiral rain band in tropical cyclones. *Tellus,* **15,** 153–161.

Yang, M.-J., D.-L. Zhang, and H.-L. Huang, 2008: A modeling study of Typhoon Nari (2001) at landfall. Part I: Topographic effects. *J. Atmos. Sci.,* **65,** 3095–3115.

Zhang, D.-L., and X. Wang, 2003: Dependence of hurricane intensity and structures on vertical resolution and time-step size. *Adv. Atmos. Sci.,* **20,** 711–725.

——, and C. Q. Kieu, 2006: Potential vorticity diagnosis of a simulated hurricane. Part II: Quasi-balanced contributions to forced secondary circulations. *J. Atmos. Sci.,* **63,** 2898–2914.

——, Y. Liu, and M. K. Yau, 2002: A multiscale numerical study of Hurricane Andrew (1992). Part V: Inner-core thermodynamics. *Mon. Wea. Rev.,* **130,** 2745–2763.

Zhong, W., D.-L. Zhang, and H. Lu, 2009: A theory for mixed vortex Rossby–gravity waves in tropical cyclones. *J. Atmos. Sci.,* **66,** 3366–3381.

Zhu, T., and D.-L. Zhang, 2006a: Numerical simulation of Hurricane Bonnie (1998). Part II: Sensitivity to cloud microphysical processes. *J. Atmos. Sci.,* **63,** 109–126.

——, and ——, 2006b: The impact of the storm-induced SST cooling on hurricane intensity. *Adv. Atmos. Sci.,* **23,** 14–22.

——, ——, and F. Weng, 2002: Impact of the Advanced Microwave Sounding Unit measurements on hurricane prediction. *Mon. Wea. Rev.,* **130,** 2416–2432.

——, ——, and ——, 2004: Numerical simulation of Hurricane Bonnie (1998). Part I: Eyewall evolution and intensity changes. *Mon. Wea. Rev.,* **132,** 225–241.